PHYSICAL REVIEW B **91**, 165404 (2015)

Electron transport in extended carbon-nanotube/metal contacts: *Ab initio* based Green function method

Artem Fediai,[1,2,*] Dmitry A. Ryndyk,[1,2,3] and Gianaurelio Cuniberti[1,2,3]
[1]*Institute for Materials Science and Max Bergman Center of Biomaterials, TU Dresden, 01062 Dresden, Germany*
[2]*Center for Advancing Electronics Dresden, TU Dresden, 01062 Dresden, Germany*
[3]*Dresden Center for Computational Materials Science, TU Dresden, 01062 Dresden, Germany*

(Received 18 December 2014; revised manuscript received 23 March 2015; published 8 April 2015)

We have developed a new method that is able to predict the electrical properties of the source and drain contacts in realistic carbon nanotube field effect transistors (CNTFETs). It is based on large-scale *ab initio* calculations combined with a Green function approach. For the first time, both internal and external parts of a realistic CNT-metal contact are taken into account at the *ab initio* level. We have developed the procedure allowing direct calculation of the self-energy for an extended contact. Within the method, it is possible to calculate the transmission coefficient through a contact of both finite and infinite length; the local density of states can be determined in both free and embedded CNT segments. We found perfect agreement with the experimental data for Pd and Al contacts. We have explained why CNTFETs with Pd electrodes are p-type FETs with ohmic contacts, which can carry current close to the ballistic limit (provided contact length is large enough), whereas in CNT-Al contacts transmission is suppressed to a significant extent, especially for holes.

DOI: 10.1103/PhysRevB.91.165404 PACS number(s): 73.63.Fg, 71.15.Mb, 73.40.Ns, 73.23.Ad

I. INTRODUCTION

Stand-alone carbon nanotubes possess uniquely high electron mobility, which makes their utilization in electronic applications attractive. This benefit is intensively used in a new family of field-effect transistors, where *semiconducting* CNTs form a channel (CNTFETs). In practice, however, the current flow through a nanotube is determined not by the high mobility in a CNT itself, but by the injection quality of the contacts. Understanding the mechanisms of the current injection in realistic CNT-metal contacts is a key to access the theoretical limit of the electron mobility in a channel of a CNTFET.

The technology of CNTFETs has passed several stages of development. Since the first demonstration [1] in 1998 for over five years, all manufactured CNTFETs necessarily had Schottky-type drain and source contacts, and operated as "Schottky barrier transistors" [2]. This significantly decreases the drain current and the efficiency of the gate control. In 2003, a CNTFET with ohmic contacts for holes was reported for the first time [3]. Further, ohmic contacts for electrons were realized using scandium [4], yttrium [5], gadolinium [6], erbium, and lanthanum [7] electrodes. Recently, a CNTFET with a 9-nm channel was manufactured and shown to have better performance than conventional metal-oxide semiconductor FETs [8]. Gate control in CNTFETs has recently been facilitated by using an all-around gate [9]; the possibility of controlling the CNTFET polarity by varying the gate material has also been shown [10].

Existing studies of metal-CNT contacts at the atomistic level still cannot explain relevant aspects of the experimental results—namely, the preferable type of conduction in CNTFET (p-, n-type, or ambipolar) and its dependence on the contact length. By the object of modeling, simulated structures can be classified as follows: (i) CNT connects to the metal by its end ("end-contact") [11]; (ii) CNT lies on the metal substrate ("side-contact") [12,13]; (iii) CNT is surrounded by the metal ("embedded contact") [14]. The most advanced works perform large-scale *ab initio* simulations, including using different types of the contacts together with a free segment of the nanotube [15–17]. This is notable as end- and side-contacts have no relevance for CNTFETs, because the former is never realized in the actual setups, and the latter has a small contact area. Indeed, *relevant CNT-metal contacts belong to the embedded type*: the nanotube is surrounded by the metal along the entire contact width and is free from the metal in the channel region.

Ab initio simulations of CNT-metal contacts were primarily aimed at estimating the electrostatic barrier between the metal and semiconducting nanotube, known as a Schottky barrier. Being developed for the contact between two bulk materials, the concept of the Schottky barrier has a clear sense and an intelligible field of application in the three-dimensional case, whereas, in the case of the metal and CNT contact, its competence is questionable. In line with this, methods of the Schottky barrier calculation are taken from conventional contacts [18] without any justification that they can be applied to the border of three- and two-dimensional materials. A review of the works dealing with the concept of the Schottky barrier can be found in Ref. [19].

Presenting an alternative to the mentioned approach are works that go beyond the Schottky barrier paradigm and characterize the injection quality of CNT-metal contacts via a combination of density functional theory (DFT) and Green function formalism [15,17,20]. However, this was done for end-contacts, leaving real experimental setups aside. The same approach has been used in Ref. [16] for a CNT embedded into the electrodes by its three periods, which does not resemble real CNT-metals contacts well.

The dependence of the contact resistance on the contact length was experimentally shown in Refs. [21,22], which

---

[*] artem.fediai@nano.tu-dresden.de

confirm that the real CNT-metal contacts belong to the extended type (with the effective contact lengths up to the order of 100 nm). Thus far, however, only a few papers have been published that deal with extended contacts. The concept of the extended contact was introduced for CNT-metal contacts in Refs. [23,24]. The extended nature of the contact in these works is taken into account by adding purely imaginary self-energy terms $-i\gamma$ to each on-site element of the tight-binding chain (it could be viewed as an "extended version" of the wide-band limit). As a reference Hamiltonian of the CNT, the empirical one was used. The single self-energy parameter $-i\gamma$ was determined by the fitting procedure. The fitting objects were the dispersion relation of the graphene on top of the single metallic layer. The parameter $-i\gamma$ was set so that the empirical Hamiltonian of the graphene, modified by $-i\gamma$, yields the same dispersion relation as those calculated using DFT. Such an estimation of the self-energy is restricted, however, to the case when the fitting procedure can be fulfilled; it is also clear that the metal can, in the general case, modify the CNT Hamiltonian arbitrarily (not only to bring an imaginary part to its diagonal elements). After all, alignment of the dispersion relation of the two systems does not mean that all their electrical properties are the same. In spite of its drawbacks, this method is the only *ab initio* based method that makes predictions on the effective contact lengths.

It should be noted that infinite extended contacts had also been treated within the *empirical* quantum models (effective mass Schroedinger equation) [25,26]. The contact Hamiltonian was modified in a way similar to the atomistic model [23,24]. In addition, it was shown that for small $-i\gamma$, the contact between the embedded and free CNT segments resembles the semiconductor junction, whereas a large $-i\gamma$ embedded CNT is fully metalized yielding Schottky contact formation. We observe both these scenarios within our *atomistic* model for Pd and Al contacts, correspondingly.

In this paper, based on earlier suggestions [23,24], we have developed a *quantitative* theory of the realistic CNT-metal contacts, taking into account advantages of the large-scale simulations [15–17]. The subject of this paper is the electrical properties of the CNT-metal contact with realistic geometry (Fig. 1), which is relevant for the state-of-the-art CNTFET technology. The novelty of this paper can be understood when compared with Refs. [23,24] as done below.

In Refs. [23,24], the self-energy of the metal is assumed to have only diagonal terms. These terms can contain only an imaginary part, which does not depend on energy (wide-band limit). The self-energy itself *was not calculated* in Refs. [23,24]; instead it was estimated using an ambitious mapping procedure. The aforementioned fitting procedure was shown to be applicable in the case of a Pd contact, but fails for a Ti contact [23], i.e., it is not universal. In our work, we perform a *direct* calculation of the self-energy, though for a simplified system, but rigorously, i.e., we define as many components of the metal self-energy matrix as we wish, both diagonal and nondiagonal, having both real and imaginary parts. Moreover, all terms of the self-energy matrix depend on energy; we have shown that this dependence can be strong and far from trivial.

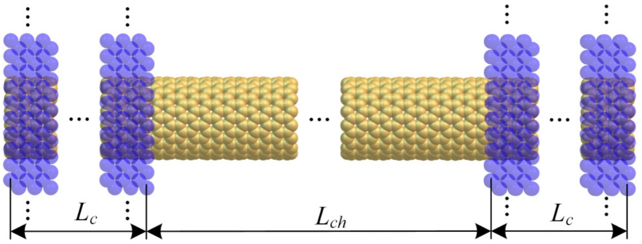

FIG. 1. (Color online) Overall system of interest includes two embedded contacts and a free CNT (16,0) segment in between. The transverse section of the contacts is infinite, whereas the contact length L_c is finite and arbitrary.

In Refs. [23–26], it was assumed that the Hamiltonian of the CNT remains unaffected by the metal. Therefore both self-energy and the Hamiltonian of the CNT cannot contain terms that describe, for example, doping of the CNT due to the vicinity of the metal and other consequences of the CNT-metal interaction. This makes it impossible to make any suggestions about the polarity of the CNTFET. In contrast, we have extracted the CNT Hamiltonian from the realistic system, which contains both an embedded and a free CNT part. This allows us to catch all possible influences of the metal on the CNT Hamiltonian, which appeared to be comparable with the changes due to the self-energy.

Our main assumption is neglecting the curvature effect of the CNT and CNT-metal interface. Within this assumption, the rest of the calculations were done rigorously. Therefore we expect to obtain reliable information about the realistic CNT-metal contact. The reliability of our method is virtually restricted by the reliability of DFT as is.

The paper is organized as follows. In Sec. II, we introduce our method. This includes a description of how and in which form the Hamiltonian of the carbon subsystem and the metal self-energy were calculated as well as how they were treated to obtain the effective Hamiltonian of the extended CNT-metal contact. Section II is closed with the description of the quantities and dependencies available for output within the method. In Sec. III, we apply our method to the CNT partially embedded into the two electrodes (Al and Pd) of the arbitrary length. We have calculated, analyzed, and compared with the experimental data, the output quantities of the method, namely, (1) the real and imaginary parts of the diagonal elements of the self-energy, (2) the transmission coefficient as a function of energy and contact length, and (3) the local density of states along the CNT and effective band edges. Finally, a short conclusion is given in Sec. IV.

II. SYSTEMATIC TREATMENT OF THE REALISTIC CNT-METAL CONTACT

The ultimate goal of this work is to treat a system consisting of a CNT partially embedded into the metallic electrodes of arbitrary width and infinite thickness (Fig. 1). As an example, we apply it to a semiconducting (16,0) CNT embedded into the metal except for a 9-nm-long channel. This system is really close to the experimental setups [8,21,22].

Two types of contacts can be distinguished in such a system. Let us introduce some terminology: (1) *internal contact* is a region close to the boundary between the embedded CNT segment and the surrounding metal. It has a cylindrical shape;

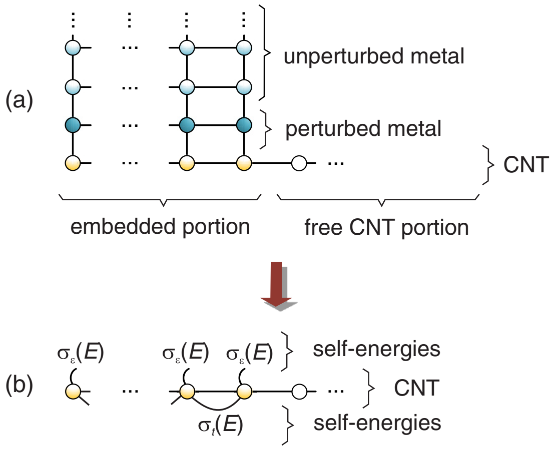

FIG. 2. (Color online) General idea of the method shown at an example of a tight-binding chain (represents CNT) connected to a two-dimensional, semi-infinite electrode (represents the three-dimensional surrounding metal): initial system, which consists of an infinite metal electrode, and a CNT (a) is to be represented by an effective system that contains only carbon atoms and metal self-energies and whose Green function is the same as for the initial system (b).

(2) the *external contact* is a region of space between embedded and free segments of the CNT, which is in the shape of a circle (Fig. 1).

Within this terminology, Refs. [15–17] consider *only* external contacts, whereas Refs. [23,24] deal with *only* internal contacts. The present work takes into account *both*.

A. The method

The general idea of this work is to bring a given system (Fig. 1) to the system, which is characterized by two components: (1) tight-binding-like Hamiltonian of the CNT, partially embedded into the metallic electrode, and (2) self-energies taking metallic electrodes into account. Figure 2 illustrates the idea of the method: an infinite system [Fig. 2(a)] that consists of the square lattice (stands for the metal) and the simple tight-binding chain (stands for the CNT) is to be substituted by the system [Fig. 2(b)] that contains only an "effective" tight-binding chain, i.e., all influence of the metal is taken into account through the self-energy terms. If the metal self-energy has been found correctly, the Green function of the effective system coincides with the corresponding part of the initial system, i.e., both systems are equivalent in terms of transport properties.

The system depicted in Fig. 2(b) is a known model system referred to as "extended contact." The novelty of this work consists not in the investigation of the extended contact model (this has already been done [23–26]), but in the correct identification of its parameters at the *ab initio* level. Then, we use Green function formalism to study the electrical properties of the extended contacts with the identified parameters.

B. Carbon subsystem

The overall infinite system of interest consists of a finite carbon subsystem ("C") and an infinite metal subsystem ("*Me*"). The corresponding Hamiltonian $\mathbf{H}$, written in the basis of the local atomic orbitals, reads

$$\mathbf{H} = \begin{bmatrix} \mathbf{H}_{\mathrm{C}} & \mathbf{T}_{\mathrm{C}-Me} \\ \mathbf{T}^{+}_{\mathrm{C}-Me} & \mathbf{H}_{Me} \end{bmatrix}. \tag{1}$$

In turn, the carbon subsystem itself consists of the left/right embedded CNT segments as well as the free CNT segment in between; the corresponding Hamiltonian reads

$$\mathbf{H}_C = \begin{bmatrix} \mathbf{H}_{\mathrm{L}} & \mathbf{T}_{LS} & \mathbf{0} \\ \mathbf{T}^{+}_{LS} & \mathbf{H}_S & \mathbf{H}_{SR} \\ \mathbf{0} & \mathbf{H}^{+}_{SR} & \mathbf{H}_R \end{bmatrix}. \tag{2}$$

Let us assume that the whole carbon subsystem is a block tight-binding chain comprising N CNT unit cells. Out of these N unit cells, N_c are embedded into the left electrode, N_s constitutes the free CNT segment, and, again, N_c are covered by the right electrode: $N = 2N_c + N_s$.

The Hamiltonian of the carbon subsystem $\mathbf{H}_{\mathrm{C}}$ can be represented as

$$\langle i|H_{\mathrm{C}}|j\rangle = \delta_{ij}h_i + \delta_{i,j+1}t_i + \delta_{j+1,i}t_i^{+} \tag{3}$$

and is completely defined by h_i and t_i. Indexes i and j are numbers of the CNT unit cells. Hereafter, the blocks of the block-tridiagonal matrices and other equal-sized matrices are set in italics, whereas all larger matrices are boldfaced.

In order to find matrices h_i and t_i, we simulate system 1 depicted in Fig. 3. By doing this, we substitute CNT, partially embedded into the metal, by its rolled-out counterpart, self-closed by periodical boundary conditions (PBC) [Fig. 4(a)]. Let us discuss this substitution in details. From the electrical point of view, system 1 with PBC can be viewed as a CNT with the curvature effects neglected. In Ref. [27], the effect of the curvature on the electrical properties of the stand-alone CNTs with different diameters/chiralities was considered. It has been shown that discrepancies in both band structure and ballistic current between the normal CNT and the corresponding nanoribbon with BPC do not exceed 7% for relevant diameters (which starts from about 1.3 nm). Moreover, Nemec *et al.* [24] have shown that fluctuation and dilution disorder effects in nonepitaxial extended contacts have very low impact on their transport properties. This means that, to a large extent, only the effective distance between the CNT and the metal plays a role. These two arguments can be considered as a justification for the usage of a "planar version" of the CNT in the identification of the CNT Hamiltonian. Besides, such substitution allows us to keep relevant π orbitals of the CNT in one direction, whereas, in real CNTs, they are always distributed among two atomic p orbitals.

Consider the geometry of system 1 in detail. System 1 consists of the 30 periods of the rolled-out (16,0) CNT, of which four periods from either side lie on top of the FCC (111) metallic lattice fragment, which is three metallic layers deep. Such a supercell is the most stable configuration of the contact between the FCC [111] metal with a lattice constant close to 4 Å (Pd and Al) and the carbon honeycomb lattice [28]. The lattice constant of the metal is changed so as to match perfectly with the honeycomb lattice within a $\sqrt{3} \times \sqrt{3}$ supercell [Fig. 5(a)]. The Pd lattice has to be scratched by 3%, whereas the Al lattice has to be 1% compressed in order to match perfectly with the honeycomb lattice (C-C distance is taken

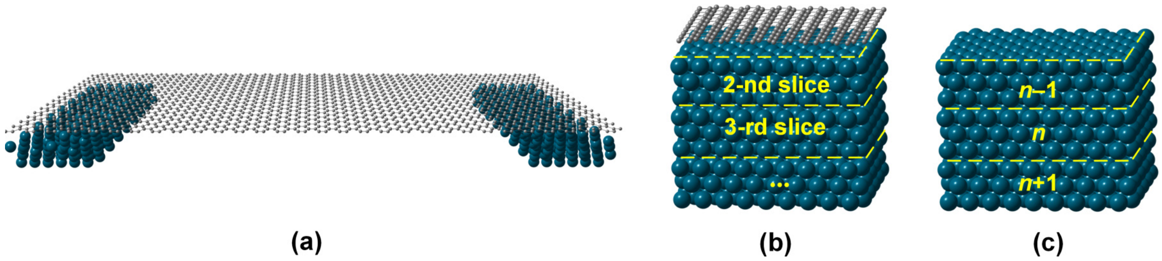

FIG. 3. (Color online) Atomic systems that have been simulated with DFT in order to obtain either elements of the Hamiltonian of the carbon subsystem or the metal self-energy: (a) *system* 1: 576 metallic atoms and 1920 C atoms [30 periods of the rolled-out CNT (16,0)]; (b) *system* 2 (810 metallic atoms and 240 carbon atoms), which consists of the four slices: carbon honeycomb lattice and three subsequent metallic slices; (c) *system* 3 (810 metallic atoms or three slices of the [111] lattice). Systems 1 and 2 contain 10 nm vacuum under the honeycomb lattice. All systems were subjected to PBC in all spatial directions.

to be 1.42 Å). We have computed the surface and bulk Green function as well as the density of states for Al [111] and Pd [111] with fully relaxed and constrained (as mentioned above) geometry. For Al, we have seen no difference for all mentioned quantities, whereas for Pd, the maximum difference does not exceed 5%. From this, we can conclude that metal-carbon interface properties remain robust against these manipulations with lattice constants. It should be noted that system 1 contains a 10-nm vacuum under the carbon sheet and is subjected to PBC in each spatial direction.

Subsystems "L", "S," and "R" of the carbon subsystem of the system 1 contain four (indices $-3\dots0$), 22 (indices $1\dots22$), and four (indices $23\dots26$) unit cells, respectively. How do we simulate the contacts comprising more than four CNT unit cells? Within DFT, we always calculate only four pairs of the elements for each of $\mathbf{H}_L$ and $\mathbf{H}_R$. The rest of the elements $(h_i,\, t_i)$ are just set to be equal to $(h_{-3},\, t_{-3})$ and (h_{26},t_{26}) for $\mathbf{H}_L$ and $\mathbf{H}_R$, correspondingly: $(h_i,t_i)\equiv(h_{-3},t_{-3})$ for $i\leqslant-4$ and $(h_i,t_i)\equiv(h_{26},t_{26})$ for $i\geqslant26$.

Out of the calculated Kohn-Sham matrix of the carbon subsystem, we take only the hopping matrix between two adjacent cells. Farther interactions are indeed vanishing. As we work in a nonorthogonal basis, we need to build the corresponding overlap matrix $\mathbf{S}_\mathrm{C}$ as well. $\mathbf{S}_\mathrm{C}$ has the same form and is built by complete analogy with $\mathbf{H}_\mathrm{C}$.

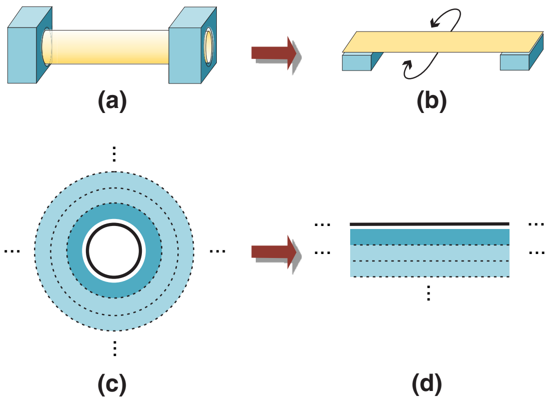

FIG. 4. (Color online) Two main assumptions of the method: (1) as a Hamiltonian of the CNT (a) we use the one for the "unrolled" CNT with PBC (b); and (2) for the metal self-energy of the CNT-metal system (c), we use the one for the system of graphene on top of a metal (d). In (b), arrows stand for PBC; in (c) and (d), dark blue denotes the part of the metal perturbed by the proximity of the carbon, in contrast to light blue, which stands for the unperturbed metal.

It is critically important that system 1 contains the transitional region between the embedded and free tube segments. This allows us to study the transition region between free and embedded segments of the tube ("external contact").

Equally important as we use system 1 to identify $\mathbf{H}_\mathrm{C}$ is that a doping of the tube by a metal is already *partially* included in $\mathbf{H}_\mathrm{C}$, which is a necessary condition to correctly describe *internal contact*. The second quantity we need to identify within internal contact is the self-energy due to interaction with the metal. Next, we describe how to do this.

C. Self-energy of metal subsystem

The left and right segments of a tube are surrounded by metallic atoms constituting electrodes. Once we find the Hamiltonians of the embedded tube and the surrounded metal, we will be able to incorporate all the influence of the metal subsystem on the carbon subsystem as follows: $\mathbf{H}^*_{L(R)}\equiv\mathbf{H}_{L(R)}+\Sigma_{L(R)}(E)$. If we substitute $\mathbf{H}_L$ and $\mathbf{H}_R$ in (2) by $\mathbf{H}^*_L$ and $\mathbf{H}^*_R$, the resulting effective system will be characterized by the same retarded Green function $\mathbf{G}^R_\mathrm{C}(E)$ as the carbon subsystem of the initial overall system [see (1)]. Such a substitution is sketched in Fig. 2. Later on, we use notation

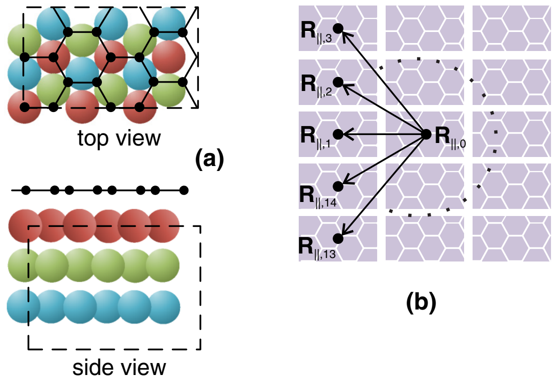

FIG. 5. (Color online) Alignment of the carbon and metal subsystems (so-called $\sqrt{3}\times\sqrt{3}$ supercell) in systems 1, 2, and 3 (a); transverse sections of systems 2 and 3 in terms of $\sqrt{3}\times\sqrt{3}$ supercells (b)

Σ instead of $\Sigma_{L(R)}$ if it is not important which electrode we mean, the left or the right one.

We have approximated the self-energy terms to be added to $\mathbf{H}_C$ by those representing a system consisting of a graphene sheet on an infinitely thick metal [Fig. 4(d)]. Such substitution should not change the magnitude of $\Sigma(E)$ significantly because the chirality of the CNT is large enough. It is also known [29] that the work function of zig-zag CNTs resembles that of graphene with a deviation of less than 2% starting from the chirality (9,0).

A "graphene on the metal" system in the $x0y$ plane has a view of the supercell (Fig. 5), translated in the x and y directions to obtain an infinite system. In the z direction, the graphene layer is followed by an infinitely thick (111) metallic slab. This system is infinite in the $x0y$ plane and semi-infinite in the z direction. Our goal is to find its metal self-energy. In general, to compute the self-energy of a system, we need to know its Hamiltonian. As the "graphene on the metal" system is (1) periodic within the $x0y$ direction and (2) approximately periodic in the z direction deep inside the metallic substrate, and (3) due to the finite range of interatomic interactions, its Hamiltonian in the LCAO basis consists of an enumerable quantity of the same elements. Our intention is to identify these elements. To do this, it is not necessary to simulate within DFT the whole infinite system. Instead, we can with high accuracy find the mentioned elements by simulating finite segments of an initial system (systems 2 and 3), as will be explained later in this section.

Along the z axis, our "graphene on the metal" system can be represented by a sequence of tightly bounded slices [see Fig. 6(a)]. Each slice, except for the first one, consists of three metallic layers; the first slice is simply a graphene sheet. Within each slice, the system is periodic in the $x0z$ plane with a common translation vectors $\mathbf{R}_{||}$ for either slice [see Fig 5(b), where a part of the "graphene on the metal" system is shown schematically].

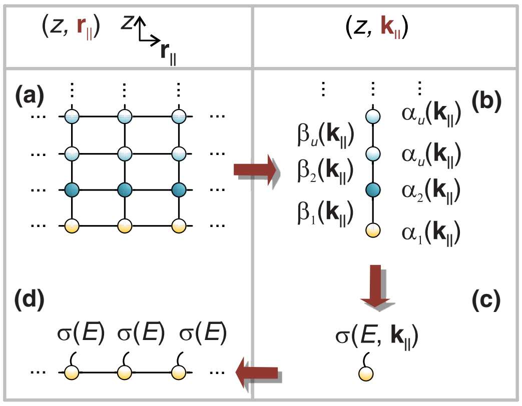

FIG. 6. (Color online) The procedure of calculation of the metal self-energy shown in an example of a simple two-dimensional lattice connected to a one-dimensional simple tight-binding chain (represents the three-dimensional metallic lattice with graphene on it): the initial system given in real space (a) can be Fourier-transformed by a transverse direction to the set of *independent* one-dimensional chains (b), which can be easily decimated to obtain the metal self-energy (c), which is then Fourier-transformed back to real space (d).

Let us consider the Hamiltonian of the "graphene on the metal" system given by its matrix elements in the local atomic orbital representation. We can define it by the set of the following matrix elements: $H_{i,a;j,b} \equiv \langle z_i,\mathbf{r}_a^{||}|H|z_j,\mathbf{r}_b^{||}|\rangle$. Hereafter, index $i(j)$ numerates slices along the z direction, whereas $a(b)$ numerates each of the transverse supercells ($x0y$ plane). Using the periodicity of the "graphene on the metal" system in the transverse direction, we can partially Fourier-transform the Hamiltonian $\mathbf{H}$ in the x and y directions to obtain its Hamiltonian in $(\mathbf{k}_{||},z)$ space, whose matrix elements are $H_{ij}(\mathbf{k}_{||}) \equiv \langle z_i|H(\mathbf{k}_{||})|z_j\rangle$. The Hamiltonian $\mathbf{H}(\mathbf{k}_{||})$ (as well as $\mathbf{H}$) describes block tight-binding chains in the z direction, but (as contrasted with $\mathbf{H}$) these chains are being completely separated in the transverse direction: $H_{ij}(\mathbf{k}_{||}) = \alpha_i(\mathbf{k}_{||})\delta_{ij} + \beta_i(\mathbf{k}_{||})\delta_{i,j+1} + \beta_i^+(\mathbf{k}_{||})\delta_{j+1,i}$. This can easily be understood by comparing Figs. 6(a) and 6(b).

The on-site and hopping matrices $\alpha_i(\mathbf{k}_{||})$ and $\beta_i(\mathbf{k}_{||})$ of the ith slice are calculated as follows [30]:

$$\alpha_i(\mathbf{k}_{||}) = \sum_{\mathbf{R}_{||}} \langle z_i|H(\mathbf{R}_{||})|z_i\rangle \exp^{\mathrm{i}\mathbf{k}_{||}\mathbf{R}_{||}}, \tag{4a}$$

$$\beta_i(\mathbf{k}_{||}) = \sum_{\mathbf{R}_{||}} \langle z_i|H(\mathbf{R}_{||})|z_{i+1}\rangle \exp^{\mathrm{i}\mathbf{k}_{||}\mathbf{R}_{||}}. \tag{4b}$$

In (4), we introduce notations $\mathbf{R}_{||} = \mathbf{r}_a^{||} - \mathbf{r}_b^{||}$ and $H(\mathbf{R}_{||}) = \langle \mathbf{r}_a^{||}|H|\mathbf{r}_b^{||}\rangle$ to denote the vector of the translation and matrix elements between a given ath cell and an arbitrary bth cell (including the ath cell itself), correspondingly [see also Fig. 5(b)]. Elements $\alpha_i(\mathbf{k}_{||})$ and $\beta_i(\mathbf{k}_{||})$ do not depend on how we have chosen the ath cell as a consequence of the transversal periodicity of each slice.

Summation by $\mathbf{R}_{||}$ can be limited by several transversal unit cells, because the elements $\langle \mathbf{r}_a^{||}|H|\mathbf{r}_b^{||}\rangle$ are decaying rapidly as $|\mathbf{r}_a^{||} - \mathbf{r}_b^{||}|$ increases. In our case, we have simulated a system that has 3×5 supercells in the $x0y$ plane [Fig. 5(b)]; thus we take 15 elements out of $\langle z_i|H(\mathbf{R}_{||})|z_i\rangle$ to find $\alpha_i(\mathbf{k}_{||})$, and the same number out of $\langle z_i|H(\mathbf{R}_{||})|z_{i+1}\rangle$ to find $\beta_i(\mathbf{k}_{||})$.

Now, we see the need to identify several elements of the form $\langle z_i|H(\mathbf{R}_{||})|z_i\rangle$ and $\langle z_i|H(\mathbf{R}_{||})|z_{i+1}\rangle$ out of the real-space Hamiltonian to perform the Fourier transformation (4). Next, we show how we do it in practice.

Assume first that each slice of the metal, starting with the second slice away of graphene, is unperturbed by proximity to the surface and has identical properties, which means that $\alpha_i(\mathbf{k}_{||}) = \alpha_u(\mathbf{k}_{||})$ and $\beta_i(\mathbf{k}_{||}) = \beta_u(\mathbf{k}_{||})$ for $i \geqslant 3$. To find $\alpha_u(\mathbf{k}_{||})$ and $\beta_u(\mathbf{k}_{||})$, we simulate a system that consists of 3×5 supercells in the transverse direction and three slices of the metal in the z direction [Fig. 3(c)]. Out of the simulated Hamiltonian matrix, we pick up the submatrices $\langle z_i|H(\mathbf{R}_{||})|z_i(z_{i+1})\rangle$ to be used in (4).

Elements $\alpha_{1(2)}(\mathbf{k}_{||})$, $\beta_{1(2)}(\mathbf{k}_{||})$ are calculated using elements extracted from the Hamiltonian of the system, which consists of the fragment of the carbon honeycomb lattice followed by the three slices of [111] FCC metallic substrate [Fig. 3(b)]. The width of each slice equals the period of the FCC lattice in (111) direction.

The transformation of the overlap matrix **S** is done in full correspondence with that of the Kohn-Sham Hamiltonian. Elements of the **S** that correspond to $\alpha_i(\mathbf{k}_{||})$ and $\beta_i(\mathbf{k}_{||})$ are denoted by $s_{\alpha,i}(\mathbf{k}_{||})$ and $s_{\beta,i}(\mathbf{k}_{||})$ accordingly.

Once we have identified the parameters of the tight-binding chain $\alpha_i(\mathbf{k}_{||})$, $\beta_i(\mathbf{k}_{||})$, $s_{\alpha,i}(\mathbf{k}_{||})$, and $s_{\beta,i}(\mathbf{k}_{||})$, we can find the metal self-energy in $(z,\mathbf{k}_{||})$ space:

$$\sigma(\mathbf{k}_{||},E) = \tau^{+}(\mathbf{k}_{||},E)g_s(\mathbf{k}_{||},E)\tau(\mathbf{k}_{||},E), \tag{5}$$

where $g_s(\mathbf{k},E)$ is the retarded surface Green function of our tight-binding chain, $\tau \equiv [Es_{\beta,1}(\mathbf{k}_{||}) - \beta_1(\mathbf{k}_{||})]$. We have used a highly converged Lopez-Sancho algorithm [31] to decimate the unperturbed metal slices and substitute them by the self-energy $\sigma_{Me}(\mathbf{k}_{||},E)$, followed by a single step of the simple decimation technique [see Eq. (5)] to obtain the $g_s(\mathbf{k}_{||},E)$ of the resulting system.

The self-energy of one *metal supercell* $\sigma(E) = \langle \mathbf{r}_a|\Sigma(E)|\mathbf{r}_a\rangle$ in the initial representation is then recovered by integrating $\sigma(\mathbf{k}_{||},E)$ over the Brillouin zone:

$$\sigma(E) = \int_{\mathbf{k}_{||}\in \mathrm{BZ}} \sigma(\mathbf{k}_{||},E)d\mathbf{k}_{||}. \tag{6}$$

D. Effective Hamiltonian of the carbon subsystem

Out of the matrix $\sigma(E)$, we extract a correction to the matrix elements of the Hamiltonian of the carbon atoms up to the third-nearest neighbor, i.e., $\langle \mathbf{r}_\alpha|\sigma(E)|\mathbf{r}_{\alpha^{(n)}}\rangle$, where $\mathbf{r}_{\alpha^{(n)}}$ is the position of the atom itself ($n = 0$), the nearest neighbor ($n = 1$), and so on.

With the elements $\langle \mathbf{r}_\alpha|\sigma(E)|\mathbf{r}_{\alpha^{(n)}}\rangle$, we construct the energy-dependent self-energy matrices $\sigma_\epsilon(E)$ and $\sigma_t(E)$ to be written down to the diagonal $h_i(\mathbf{k}_{||})$ and nondiagonal $t_i(\mathbf{k}_{||})$ elements of the Hamiltonian of the embedded CNT, correspondingly. This means that we are beyond the wide-band limit, which was used for extended contacts earlier [23,24]. More important is that we correct both real and imaginary parts of the on-site h_i and hopping t_i elements of the CNT Hamiltonian of the contact to obtain their effective counterparts h_i^* and t_i^*: $h_i^*(E) = h_i + \sigma_h(E), t_i(E)^* = t_i + \sigma_t(E)$. As a result, we obtain a finite chain of the tightly bounded CNT unit cells, which are connected to the reservoirs in a distributed manner as shown in Fig. 2(b). It is then decimated cell by cell to obtain the self-energies of the left and right contacts [23,24] $\sigma_L(E)$ and $\sigma_R(E)$, which are of the same size as h_i and bounded by the first and the last on-site matrices of the quantum system.

At this point, it is possible to find the retarded Green function of the quantum system $\mathbf{G}_S^R(E)$ in a conventional way:

$$\mathbf{G}_S^R(E) = \frac{1}{(E+\mathrm{i}\eta)\mathbf{S}_S - \mathbf{H}_S^*}, \tag{7}$$

where $\mathbf{H}_S^*$ is the effective Hamiltonian of the quantum system. It coincides with $\mathbf{H}_S$, except for the two elements, namely, $\langle 1|H_S^*|1\rangle \equiv \langle 1|H_S|1\rangle + \sigma_L$ and $\langle N_s|H_S^*|N_s\rangle \equiv \langle N_s|H_S|N_s\rangle + \sigma_R$; η is a positive infinitesimal. Hereafter, we omit the superscript "S" of the Green function of the quantum system for convenience.

E. Output of the method

We are focusing mainly on the two physical quantities to analyze the CNT-metal contact quantitatively: (*) the transmission coefficient between the left and right electrodes $T(E)$ (including its dependence on contact length) and (**) the local density of states both being defined by the Green function of the quantum system $\mathbf{G}^R(E)$ and the electrodes' self-energies $\sigma_{L(R)}(E)$.

We avoid inverting the full matrix in Eq. (7) to find the Green function $\mathbf{G}^R(E)$. Instead, we use the recursive Green function method [32], which allows us to find G^R_{1,N_s} as well as $G^R_{i,i}$, which are the only necessary elements of $\mathbf{G}^R$ for calculating the transmission coefficient and the local density of states (LDOS).

1. *Transmission coefficient*

After calculation of the so-called broadening matrices $\gamma_{L(R)} = -2\mathrm{Im}\sigma_{L(R)}$ and the retarded Green function $\mathbf{G}^R$, we are able to calculate the transmission coefficient from the left to the right contact using the Fisher-Lee relation [33], which reads for our block tight-binding system:

$$T(E) = \mathrm{Tr}\big[\gamma_L(E)G^R_{1,N_s}(E)\gamma_R(E)G^A_{1,N_s}(E)\big]. \tag{8}$$

2. *Local density of states along the CNT*

The local density of states can be defined for each CNT unit cell as follows [34]:

$$\rho_i(E) = -\frac{2}{\pi}\,\mathrm{Im}\,\mathrm{Tr}[G^R(E)S]_{i,i}, \tag{9}$$

where S stands for the overlap matrix of the quantum region; factor 2 stands for the spin.

In order to study the external contact, it is important to visualize the LDOS in the embedded part of the tube. To do this, we expand the length of the quantum region so as to enclose additionally four periods of the CNT from each side of the uncovered tube segment. The calculation of the Green function in this case is the same except for stopping the decimation four CNT cells earlier.

3. *Effective band profile of the CNT-metal junctions*

The profiles of the conduction and the valence band edges, E_c and E_v, in conventional semiconductor junctions, provide the most essential information on contact properties. Band edges can be defined once the dispersion relations $E(\mathbf{k})$ have been found. Although $E(\mathbf{k})$ can strictly be defined for the periodical systems only, it is also used for "almost" periodical systems (p-n junctions) as well as for systems with clearly broken periodicity (heterojunctions).

In our work, we define effective band edges $E_c(z)$ and $E_v(z)$ for each ith CNT unit cell from the dispersion relation $E_i(k_z)$ defined for the ith auxiliary system, comprising the infinite tight-binding chain given by the on-site matrices h_i and the hopping matrices t_i (for the free CNT segment) and h_i^* and t_i^* for the embedded CNT segment (together with the corresponding overlap matrices $s_{h,i}$ and $s_{t,i}$). Hereafter, the z direction coincides with the tube axis.

The above-mentioned auxiliary systems have the Hermitian (non-Hermitian) Hamiltonian for the free (embedded) CNT segment. In the second case, the self-energies $E_i(k_z)$ have both real and imaginary parts. The former are the positions of the metastable energy levels, whereas the latter describes their broadening. Band edges, if any, are determined solely by the real part of the self-energies as the edges of the forbidden band.

III. RESULTS FOR ALUMINUM AND PALLADIUM CONTACTS

We apply the method described above to analyze the injection properties of the Pd and Al extended contacts as well as to compare qualitatively our results with the existing experiments. Qualitative comparison can be done by analyzing the transmission coefficient, the density of states and the band profiles at equilibrium. For example, the position of the Fermi level relative to band edges at equilibrium tells us the preferable polarity of the CNTFET; the dependence of the contact resistance on contact length can be estimated by analyzing the transmission coefficient $T(E)$ at different contact lengths.

The geometries of the systems that were used to find the necessary elements of the overlap matrices and Kohn-Sham Hamiltonians were introduced earlier. Within these geometries, we have taken the distance between the top layer of the metals and carbon sheet from Ref. [35]: $d_{\text{C-Al}} = 3.72$ Å, $d_{\text{C-Pd}} = 3.50$ Å, i.e., we assume that the CNT-metal distance equals that between graphene and the metal. This approximation cannot cover the real geometry of the CNT-metal contact and the wetting properties of the particular metal (which are shown to be different [36]), but it is based on the special van der Waals functional, which is claimed to give reliable results for the metal-carbon interface [35]. Besides, it is perfectly compatible with the approximations we have accepted for the carbon subsystem Hamiltonian and the metal self-energy. Although the CNT-metal distances have also been defined by DFT simulations [12,14,15], both methods of its definition and the type of the functional used seem to be less reliable. For Pd, these studies give the carbon-metal distance $\approx$2.2 Å; as we used this magnitude in our calculations of CNT-Pd contact, we have observed no signs of the extended character of the contacts and the n-type doping of the embedded tube segment. Both these findings are in strong contradiction with all experimental data with which we are familiar.

The Kohn-Sham Hamiltonians and the overlap matrices of the systems 1–3 (Fig. 3) were obtained with the use of DFT as implemented in the Quickstep module of the CP2K package [37]. Within the energy functional, we use the Goedecker, Teter, and Hutter (GTH) approximation of the pseudoptentials [38,39]. To approximate the exchange-correlation energy, the meta-generalized gradient approximation (GGA) of Perdue, Burke, and Ernzerhof (PBE) [40] was used. In order to express the systems' Hamiltonians in the local atomic orbital representation, we used a single-ζ valence basis set for C atoms ($2s$, $2p_x$, $2p_y$, $2p_z$ orbitals) and a double-ζ valence basis set plus the polarization function for Pd (25 orbitals in total) and Al (13 orbitals in total). This allows us to include individual features of each of the metals in detail, keeping only four orbitals per C atom at the final stage of calculations.

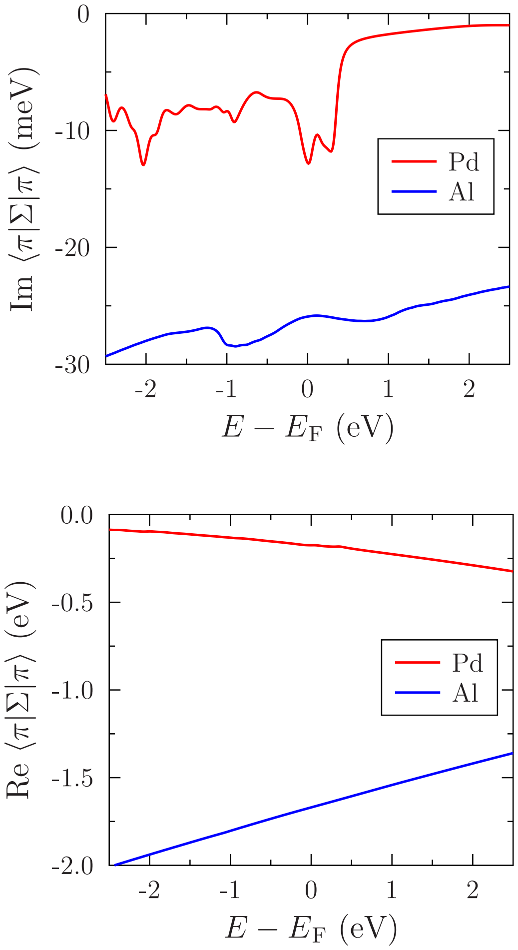

FIG. 7. (Color online) Averaged diagonal elements of the self-energy taken between π orbitals of the same C atoms: (a) imaginary and (b) real parts for both Pd and Al.

A. Self-energies of metal subsystem for Al and Pd contacts

Within our model, the presence of the metal around the embedded CNT segments is taken into account in a twofold manner: (*) by modification of the $\mathbf{H}_\mathrm{C}$ itself due to proximity of the metal and (**) further modification of the $\mathbf{H}_\mathrm{C}$ by summing up with the self-energy. The self-energies contain elements that modify all on-site and hopping elements within a carbon atom and those between the nearest, next-nearest, and the atom behind the latter.

The real and imaginary parts of the most important matrix element $\langle\pi|\Sigma(E)|\pi\rangle$ of the metal's self-energy matrix are plotted in Fig. 7. It is worth noting that the other elements of $\Sigma(E)$ have the same or a lower order than the former. Together with the changes in the carbon subsystem's Hamiltonian, four elements $\langle\mathbf{r}_\alpha|\sigma(E)|\mathbf{r}_{\alpha^{(n)}}\rangle$ $(n = 0,1,2,3)$ contain exhaustive information about the extended metal-CNT contact.

In order to calculate the metal self-energies, we evaluate the integrand in Eq. (6) at 21×36 and 31×54 uniformly distributed k points for Al and Pd, respectively. During the calculation of the retarded surface Green function of the unperturbed metal we set the infinitesimal η to be 5×10^{-2} eV; for the last (perturbed) slice of the metal the infinitesimal has been taken to be 10^{-3} eV. In both cases, the corresponding value is about one order less than the imaginary part of the self-energy; therefore, it does not change the resulting Green function significantly while making it possible to bypass Green function singularities.

Since the periodicity of the metals does not match with those of the carbon, we can distinguish four different carbon atoms in terms of the perturbation due to the metal. In Fig. 7, the matrix elements of self-energies $\langle\pi|\Sigma|\pi\rangle$ averaged over these four kinds of carbon atoms are shown.

In the wide-band limit, it was shown [23,24] that a small imaginary part preserves the high conductance of the contact if the contact is sufficiently long. In contrast, a large imaginary part suppresses conduction for long contacts, but for short contacts it yields lower contact resistance. Although the Al-CNT distance is slightly larger than that of Pd-CNT, the element $\mathrm{Im}\langle\pi|\Sigma(E)|\pi\rangle$ in the relevant energy range is three to 10 times larger than those of the Pd contact.

Although the self-energy elements are significant for all four carbon orbitals, in the relevant energy range, only the modification of the π orbitals plays a role. Inclusion of the three other σ-like orbitals into consideration does not change the transmission coefficient and density of states in the relevant energy range.

B. Transmission coefficient as a function of contact length

The dependence of the transmission coefficient on the contact length (expressed in the number of the unit cells N_c of the CNT) is shown in Fig. 8. First, let us analyze it for the infinitely long contact. For both Al and Pd contacts, we have an energy gap of almost 1 eV, where the transmission is completely suppressed. For the infinitely long Pd contact, the transmission virtually reaches a ballistic limit away from this gap, whereas the Al contact suppresses conduction, especially for holes. For Pd contacts, the Fermi level is shifting as if it were p-type doped. For Al contacts, it is not clear from the transmission coefficient plot, if there is any doping or not. Doping-related issues are clearer from the LDOS, which is discussed below.

As for the dependence of the transmission on the contact length, we observe two main trends. First, for the Al contact, more than 50% of the possible injection efficiency is reached for as short a contact as 2.13 nm (five CNT periods). The palladium contact is much more extended: the transmission coefficient continues to grow till the contact length reaches 42.6 nm, whereas *short Pd contacts are even worse than a short Al contact*. These findings agree with the work of Nemec *et al.* [23,24] as the imaginary part of the self-energy for the Al contact is three to 10 times larger than those of the Pd contact. We can also see the consequences of the sharp drop of the $\mathrm{Im}\,\langle\pi|\Sigma(E)|\pi\rangle$ at the plot of $T(E)$ for Pd: for electrons (i.e., $E > E_F$) longer Pd contacts are necessary to achieve its maximal value.

For Al contacts, $\mathrm{Im}\langle\pi|\Sigma(E)|\pi\rangle$ varies slowly with energy wherewith it reminds the wide-band limit. Hence we expect the transmission to change uniformly. Deeper suppression of the holes' conductivity is observed compared with those of electrons instead. This could find a possible explanation during the analysis of LDOS, which is given below.

C. Local density of states along the nanotube

The local density of states along the nanotube with Pd and Al contacts was determined according to Eq. (9) and plotted together with the effective band edges in Fig. 9. These plots can be used to analyze the external contact, i.e., the contact between the embedded and free tube segments.

Consider first the LDOS in the embedded part of the nanotube. For the Pd contact, we clearly see metal-induced p-type doping, which resembles the doping of graphene [28]. The CNT embedded into the Al contact, in contrast, is losing its band gap and is becoming metallic. Which states are filled, propagating, or localized? The effective dispersion relation shows that there is no band gap in the embedded part of the tube; therefore, the Al contact is truly metallic, i.e., the band gap of the pristine CNT is filled by propagating states. It should be noted that the sign and magnitude of the CNT doping by Pd agree with those for graphene [28]. For Al, they are not comparable, because on being introduced into Al, CNT changes its effective band structure drastically.

The electrical properties of the free CNT part also differ for Pd and Al contacts. P-type doping of the Pd contact extends to the free CNT segments as well, while the free part of

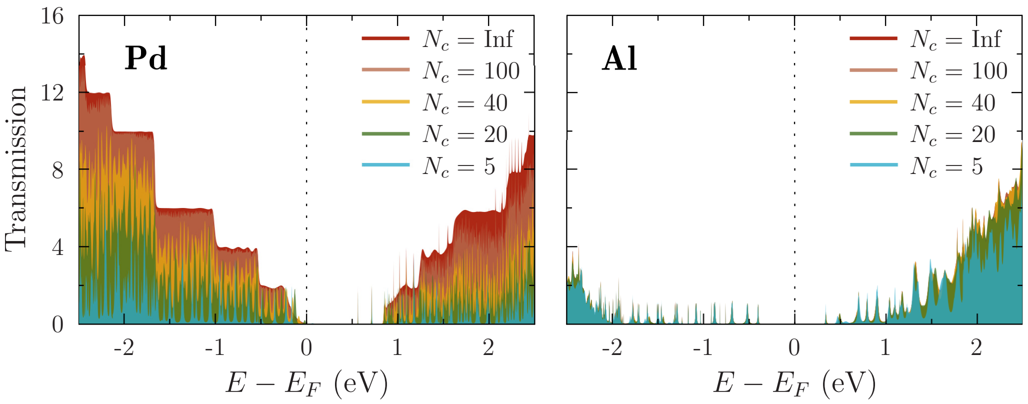

FIG. 8. (Color online) Transmission coefficient as a function of energy for different contact lengths for Pd and Al contacts. Contact length is expressed in the number of CNT unit cells N_c

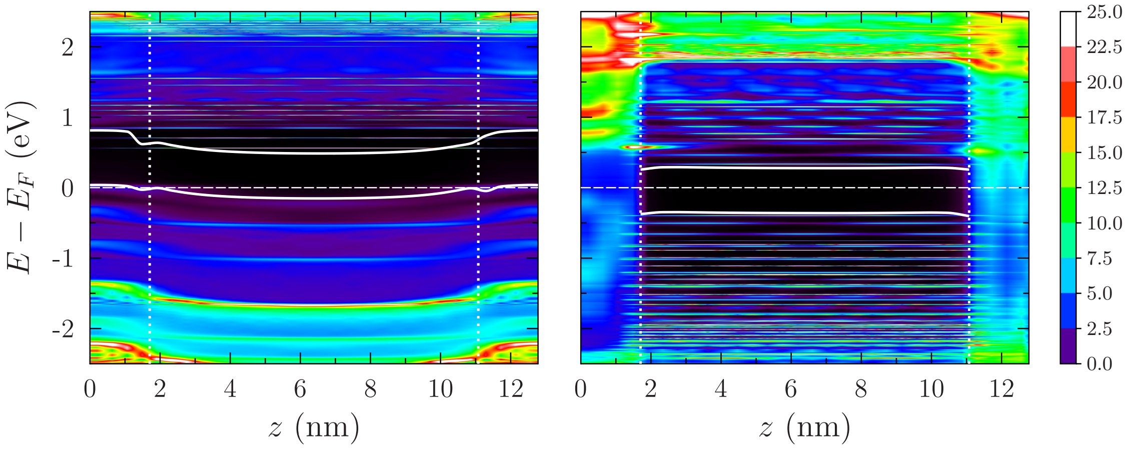

FIG. 9. (Color online) Local density of states along CNT, including four embedded unit cells from both sides (color map is given in eV^{-1}). Solid white lines denote valence and conduction bands; dotted lines indicate the border between embedded and free CNT segments. Left (right) graph stands for Pd (Al) contact.

Al-contacted CNT remains undoped. In both cases, however, there is no evidence that the effective band structure of the free CNT segment suffers any changes compared with those of pristine CNT except doping.

In principle, the effective band edges could give us information on the presence/absence of a Schottky barrier in the z direction between the embedded and free CNT segments (which we refer to as the external contact). From Fig. 9, we can conclude that the Schottky barrier height for the external Pd contact is close to zero for holes. This assumption is also confirmed by the transmission coefficient behavior, which reaches the quantum limit below the Fermi level (Fig. 8).

From the band edges' positions near the CNT-Al contact (Fig. 9), we can conclude that equal Schottky barriers exist for both holes and electrons. At the same time, the position of the quasidiscrete states below the valence band edge along with the damping of the transmission coefficient within the refereed energy range allows us to assume that there is a narrow and high electrostatic barrier for holes between the CNT segment embedded into the Al contact and the free one. It should be noted that the band edges were defined for a set of discrete points with a spacing ≈ 0.43 Å (one period of CNT). Therefore it is impossible to identify electrostatic barriers (even if they exist) shorter than the period of the CNT. It is likely, however, that in the case of Al, we deal with this. One can assume that the height of this barrier should be as large as the real part of the self-energy element $\langle\pi|\Sigma|\pi\rangle$, which is ≈ 2 eV. Therefore the injection quality of the Al contact is low due to both internal and external contacts.

D. Relation to the experimental results

We have intentionally chosen the most different (in terms of the experimental behavior) contact materials to verify the method. Palladium is a material that is known to be able to form an ohmic contact with CNTs yielding conduction close to the ballistic limit [3]; it is also a well-established fact that CNTFETs with Pd electrodes are pronounced p-type FETs. The effective contact length of the Pd contact in experiments has an order of 100 nm just like in our calculations. At the same time, Al-contacted CNTFETs experimentally manifest mainly electron conduction with signs of ambipolarity. The current that the Al-contacted CNT can carry is several orders less than that of the Pd-contacted tube.

The above-described experimental results agree qualitatively with the existing experimental data [3,8,21,22,41,42] both in terms of the preferable conduction type and difference in the current flow magnitude. First, consider the case of the infinitely long contact (in practice, this means that $L_c \gtrsim 100$ nm [22]). The position of the Fermi level in relation to band edges (Fig. 9) in the case of Pd contact assumes that the transfer characteristic of the CNTFET with Pd contacts must be asymmetric, namely, negative gate voltage must yield a higher drain current than positive gate voltage. This is what was actually observed for Pd-contacted CNTFETs in practice (see, for instance, Fig. 2(b) in Ref. [8]). It is important to note that the experimental setup [8] has a channel length $L_{\text{ch}} \approx 9$ nm and tube diameter $d_{\text{CNT}} \approx 1.3$ nm, which resembles closely the structure we simulate in this work [$d_{\text{CNT}} = 1.25$ nm (diameter of (16,0) CNT); $L_{\text{ch}} = 9.4$ nm].

There are no available experimental data on short-channel Al-contacted CNTFET, whose L_{ch} and d_{CNT} resemble those of the structure we simulate. There are, however, available transfer I-V characteristics for single-CNT CNTFET with $d_{\text{CNT}} \approx 2.5$ nm and $L_{\text{ch}} = 2500$ nm [42] (see Fig. 4(a) in Ref. [42]), as well as for single-CNT CNTFET with $L_{\text{ch}} = 1200$ nm [41] and unknown diameter [41] (see Fig. 1(d) in Ref. [41]). Both these Al-contacted CNTFETs possess n-type conduction as the preferable one. How can we compare it with our results? In Fig. 8, the transmission coefficient for electrons ($E > 0$) is much higher than for holes ($E < 0$). We expect, therefore, for the theoretical transfer characteristics to have asymmetry that is typical for the n-type CNTFET. Thus, Al-contacted CNTFETs are n-type FET both according to our theory and in practice. In Ref. [41], based on experimental results, the authors suggest that Al-contacted CNTFETs have Schottky barriers for both types of carriers; higher for holes and smaller for electrons. The calculated band edges depicted in Fig. 9 confirm this assumption as well.

As reported in Ref. [41] [see Figs. 1(b) and 1(d) inside], the drain current difference between Al- and Pd-contacted CNTFETs exceeds one order of magnitude. This agrees qualitatively with our results for $T(E)$ for Al- and Pd-contacted CNT (Fig. 8): the transmission of a Pd-CNT contact tends to the ballistic limit, whereas that of an Al-CNT contact is strongly suppressed. We expect, therefore, similar differences in the drain current.

As reported in Ref. [8], the drain current of Pd-contacted CNTFETs depends on the contact length. The drain current increases as L_c increases, and reaches its maximal magnitude for $L_c \gtrsim 100$ nm. In our calculations, the transmission coefficient $T(E,L_c)$ smoothly tends to the ballistic limit as L_c grows (Fig. 8). At $N_c = 100$ (which corresponds to length $L_c = 42.6$ nm), our model predicts virtually complete transmission saturation. This suggests that the drain current will depend on L_c in the same way as in the experiment. For Al contact, we cannot make similar comparisons due to the absence of a corresponding experiment. Being only qualitative, such a good agreement with experimental data, has never been achieved at the *ab initio* level before.

IV. CONCLUSION

For the first time, we consider realistic CNT-metal contacts in CNTFET. By this, we mean that both internal (extended region between the embedded CNT segment and a metal) and external (well-localized region near the contact of the free and embedded CNT segments) contacts were taken into account. Previous works consider either internal contacts [23–26] or external contacts solely [16], but never both.

Our method contains two stages. At the first stage, we identify all the elements of the Hamiltonian and overlap matrices of the CNT partially embedded into the metal. For this, we simulate one principal system (system 1) and two auxiliary systems (systems 2 and 3). During the second stage, we substitute the metal subsystem by the set of the distributed self-energy terms that are to be added to the Hamiltonian of the carbon subsystem of the system 1. In fact, we have generalized the conventional method of incorporating infinite electrodes trough self-energies [34] to the case of extended electrodes. Self-energy terms for extended contacts have never been calculated before this; in the best case, they have been identified by fitting the $E(\mathbf{k})$ relation of a graphene sheet on a metal [23,24] or just setting it arbitrarily [25,26].

As we looked for self-energies of the metallic electrodes, we had partially switched to $\mathbf{k}$ space (in the transverse direction) and gone back to the initial representation. For this, we used auxiliary periodic systems that have a common period in the transversal direction in both the carbon and the metal.

We have introduced a wider spectrum of output quantities, including DOS and effective band edges as a function of position along the tube (including the embedded part), as well as a transmission coefficient depending on the length of the contact.

To check the prediction abilities of the method, we have applied it to CNT-Al and CNT-Pd contacts. For Pd contacts, we observe p-type doping of the embedded and free segments of the tube; the contact has an effective width of the order of 100 nm. Long Pd contacts manifest a transmission close to the ballistic limit, whereas the transmission in the short Pd contacts is strongly suppressed. These results agree perfectly with the experimental data on Pd contacts [3,8,21,22,42].

The aluminum-CNT contact manifests, in some sense, opposite electrical properties compared to the Pd-CNT one. First of all, the embedded tube turns out to be fully filled by the propagating states. At the same time, the transmission is suppressed for holes, which is presumably attributed to a short and high Schottky barrier at the external contact. The internal contact indeed has a high resistance for both electrons and holes. This agrees well with the existing experimental data, which show that Al-contacted CNTFETs are n-FETs [41]. The elongation of the Al contact is idle, because 50% of the transmission maximum is still being achieved for the 2-nm-long contact. The transmission coefficient at a relevant energy range is well below the ballistic limit, which agrees with the existing experiment [41] as well.

ACKNOWLEDGMENTS

Fruitful discussions with D. Nozaki, A. Kleshchonok, M. Claus, V. Bezugly, A. Dianat, and R. Gutierrez (TU Dresden) are gratefully acknowledged. We acknowledge the Center for Information Services and High Performance Computing (ZIH) at TU Dresden for computational resources. This work is partly supported by the German Research Foundation (DFG) within the Cluster of Excellence "Center for Advancing Electronics Dresden." It was also partly funded by the EU within the project CARbon nanoTube phOtONic devices on silicon (CARTOON, Project No. 618025).

---

[1] S. J. Tans, A. R. M. Verschueren, and C. Dekker, Room-temperature transistor based on a single carbon nanotube, Nature (London) **393**, 49 (1998).

[2] S. Heinze, J. Tersoff, R. Martel, V. Derycke, J. Appenzeller, and P. Avouris, Carbon nanotubes as schottky barrier transistors, Phys. Rev. Lett. **89**, 106801 (2002).

[3] A. Javey, J. Guo, Q. Wang, M. Lundstrom, and H. Dai, Ballistic carbon nanotube field-effect transistors, Nature (London) **424**, 654 (2003).

[4] L. Ding, S. Wang, Z. Zhang, Q. Zeng, Z. Wang, T. Pei, L. Yang, X. Liang, J. Shen, Q. Chen, R. Cui, Y. Li, and L.-M. Peng, Y-contacted high-performance n-type single-walled carbon nanotube field-effect transistors: Scaling and comparison with Sc-contacted devices, Nano Lett. **9**, 4209 (2009).

[5] Z. Zhang, X. Liang, S. Wang, K. Yao, Y. Hu, Y. Zhu, Q. Chen, W. Zhou, Y. Li, Y. Yao, J. Zhang, and L.-M. Peng, Doping-free fabrication of carbon nanotube based ballistic CMOS devices and circuits, Nano Lett. **7**, 3603 (2007).

[6] C. Wang, K. Ryu, A. Badmaev, J. Zhang, and C. Zhou, Metal contact engineering and registration-free fabrication of complementary metal-oxide semiconductor integrated circuits using aligned carbon nanotubes, ACS Nano **5**, 1147 (2011).

[7] D. Shahrjerdi, A. D. Franklin, S. Oida, J. A. Ott, G. S. Tulevski, and W. Haensch, High-performance air-stable n-type carbon nanotube transistors with erbium contacts, ACS Nano **7**, 8303 (2013).

[8] A. D. Franklin, M. Luisier, S.-J. Han, G. Tulevski, C. M. Breslin, L. Gignac, M. S. Lundstrom, and W. Haensch, Sub-10 nm carbon nanotube transistor, Nano Lett. **12**, 758 (2012).

[9] Z. Chen, D. Farmer, S. Xu, R. Gordon, P. Avouris, and J. Appenzeller, Externally assembled gate-all-around carbon nanotube field-effect transistor, IEEE Electron Device Lett. **29**, 183 (2008).

[10] A. D. Franklin, S. O. Koswatta, D. B. Farmer, J. T. Smith, L. Gignac, C. M. Breslin, S.-J. Han, G. S. Tulevski, H. Miyazoe, W. Haensch, and J. Tersoff, Carbon nanotube complementary wrap-gate transistors, Nano Lett. **13**, 2490 (2013).

[11] Y. He, J. Zhang, S. Hou, Y. Wang, and Z. Yu, Schottky barrier formation at metal electrodes and semiconducting carbon nanotubes, Appl. Phys. Lett. **94**, 093107 (2009).

[12] B. Shan and K. Cho, Ab initio study of schottky barriers at metal-nanotube contacts, Phys. Rev. B **70**, 233405 (2004).

[13] T. Meng, C.-Y. Wang, and S.-Y. Wang, First-principles study of contact between Ti surface and semiconducting carbon nanotube, J. Appl. Phys. **102**, 013709 (2007).

[14] W. Zhu and E. Kaxiras, The nature of contact between Pd leads and semiconducting carbon nanotubes, Nano Lett. **6**, 1415 (2006).

[15] J. J. Palacios, P. Tarakeshwar, and D. M. Kim, Metal contacts in carbon nanotube field-effect transistors: Beyond the Schottky barrier paradigm, Phys. Rev. B **77**, 113403 (2008).

[16] C. Adessi, R. Avriller, X. Blase, A. Bournel, H. C. d'Honincthun, P. Dollfus, S. Frégonèse, S. Galdin-Retailleau, A. López-Bezanilla, C. Maneux, H. N. Nguyen, D. Querlioz, S. Roche, F. Triozon, and T. Zimmer, Multiscale simulation of carbon nanotube devices, C. R. Phys. **10**, 305 (2009).

[17] Y.-H. Kim and H. S. Kim, Anomalous length scaling of carbon nanotube-metal contact resistance: An ab initio study, Appl. Phys. Lett. **100**, 213113 (2012).

[18] R. T. Tung, Formation of an electric dipole at metal-semiconductor interfaces, Phys. Rev. B **64**, 205310 (2001).

[19] J. Svensson and E. E. B. Campbell, Schottky barriers in carbon nanotube-metal contacts, J. Appl. Phys. **110**, 111101 (2011).

[20] A. Zienert, J. Schuster, and T. Gessner, Metallic carbon nanotubes with metal contacts: Electronic structure and transport, Nanotechnol. **25**, 425203 (2014).

[21] A. D. Franklin and Z. Chen, Length scaling of carbon nanotube transistors, Nat. Nano **5**, 858 (2010).

[22] A. D. Franklin, D. B. Farmer, and W. Haensch, Defining and overcoming the contact resistance challenge in scaled carbon nanotube transistors, ACS Nano **8**, 7333 (2014).

[23] N. Nemec, D. Tománek, and G. Cuniberti, Contact dependence of carrier injection in carbon nanotubes: An ab initio study, Phys. Rev. Lett. **96**, 076802 (2006).

[24] N. Nemec, D. Tománek, and G. Cuniberti, Modeling extended contacts for nanotube and graphene devices, Phys. Rev. B **77**, 125420 (2008).

[25] J. Knoch, S. Mantl, Y.-M. Lin, Z. Chen, P. Avouris, and J. Appenzeller, An extended model for carbon nanotube field-effect transistors, in *62nd Device Research Conference (DRC)' 2004* [Includes "Late News Papers" volume] (IEEE, Piscataway, NJ, 2004), pp. 135–136.

[26] J. Knoch and J. Appenzeller, Tunneling phenomena in carbon nanotube field-effect transistors, Phys. Status Solidi A **205**, 679 (2008).

[27] V. Bezugly, H. Eckert, J. Kunstmann, F. Kemmerich, H. Meskine, and G. Cuniberti, Quantification of curvature effects in boron and carbon nanotubes: Band structures and ballistic current, Phys. Rev. B **87**, 245409 (2013).

[28] G. Giovannetti, P. A. Khomyakov, G. Brocks, V. M. Karpan, J. van den Brink, and P. J. Kelly, Doping graphene with metal contacts, Phys. Rev. Lett. **101**, 026803 (2008).

[29] W. S. Su, T. C. Leung, and C. T. Chan, Work function of single-walled and multiwalled carbon nanotubes: First-principles study, Phys. Rev. B **76**, 235413 (2007).

[30] P. Damle, A. W. Ghosh, and S. Datta, First-principles analysis of molecular conduction using quantum chemistry software, Chem. Phys. **281**, 171 (2002).

[31] M. P. L. Sancho, J. M. L. Sancho, J. M. L. Sancho, and J. Rubio, Highly convergent schemes for the calculation of bulk and surface green functions, J. Phys. F **15**, 851 (1985).

[32] R. Lake, G. Klimeck, R. C. Bowen, and D. Jovanovic, Single and multiband modeling of quantum electron transport through layered semiconductor devices, J. Appl. Phys. **81**, 7845 (1997).

[33] D. S. Fisher and P. A. Lee, Relation between conductivity and transmission matrix, Phys. Rev. B **23**, 6851 (1981).

[34] Y. Xue, S. Datta, and M. A. Ratner, First-principles based matrix green's function approach to molecular electronic devices: General formalism, Chem. Phys. **281**, 151 (2002).

[35] M. Vanin, J. J. Mortensen, A. K. Kelkkanen, J. M. Garcia-Lastra, K. S. Thygesen, and K. W. Jacobsen, Graphene on metals: A van der waals density functional study, Phys. Rev. B **81**, 081408 (2010).

[36] Y. Zhang, N. W. Franklin, R. J. Chen, and H. Dai, Metal coating on suspended carbon nanotubes and its implication to metaltube interaction, Chem. Phys. Lett. **331**, 35 (2000).

[37] J. VandeVondele, M. Krack, F. Mohamed, M. Parrinello, T. Chassaing, and J. Hutter, Quickstep: Fast and accurate density functional calculations using a mixed Gaussian and plane waves approach, Comput. Phys. Commun. **167**, 103 (2005).

[38] S. Goedecker, M. Teter, and J. Hutter, Separable dual-space Gaussian pseudopotentials, Phys. Rev. B **54**, 1703 (1996).

[39] C. Hartwigsen, S. Goedecker, and J. Hutter, Relativistic separable dual-space Gaussian pseudopotentials from H to Rn, Phys. Rev. B **58**, 3641 (1998).

[40] J. P. Perdew, K. Burke, and M. Ernzerhof, Generalized gradient approximation made simple, Phys. Rev. Lett. **77**, 3865 (1996).

[41] M. H. Yang, K. B. K. Teo, W. I. Milne, and D. G. Hasko, Carbon nanotube Schottky diode and directionally dependent field-effect transistor using asymmetrical contacts, Appl. Phys. Lett. **87**, 253116 (2005).

[42] A. Javey, Q. Wang, W. Kim, and H. Dai, Advancements in complementary carbon nanotube field-effect transistors, in *International Electron Devices Meeting (IEDM '03) Technical Digest* (IEEE, Piscataway, NJ, 2003), pp. 31.2.1–31.2.4.